Published in final edited form as:

J Am Chem Soc. 2018 September 19; 140(37): 11686–11697. doi:10.1021/jacs.8b05514.

Near-Infrared Photoactivatable Nitric Oxide Donors with Integrated Photoacoustic Monitoring

Effie Y. Zhou[†,§], **Hailey J. Knox**[†,§], **Christopher J. Reinhardt**[†], **Gina Partipilo**[†], **Mark J. Nilges**[‡], **Jefferson Chan**[*,†]

[†]Department of Chemistry and Beckman Institute for Advanced Science and Technology, Urbana, Illinois 61801, United States

[‡]Illinois EPR Research Center, University of Illinois at Urbana–Champaign, Urbana, Illinois 61801, United States

Abstract

Photoacoustic (PA) tomography is a noninvasive technology that utilizes near-infrared (NIR) excitation and ultrasonic detection to image biological tissue at centimeter depths. While several activatable small-molecule PA sensors have been developed for various analytes, the use of PA molecules for deep-tissue analyte delivery and monitoring remains an underexplored area of research. Herein, we describe the synthesis, characterization, and *in vivo* validation of photoNOD-1 and photoNOD-2, the first organic, NIR-photocontrolled nitric oxide (NO) donors that incorporate a PA readout of analyte release. These molecules consist of an aza-BODIPY dye appended with an aryl *N*-nitrosamine NO-donating moiety. The photoNODs exhibit chemostability to various biological stimuli, including redox-active metals and CYP450 enzymes, and demonstrate negligible cytotoxicity in the absence of irradiation. Upon single-photon NIR irradiation, photoNOD-1 and photoNOD-2 release NO as well as rNOD-1 or rNOD-2, PA-active products that enable ratiometric monitoring of NO release. Our *in vitro* studies show that, upon irradiation, photoNOD-1 and photoNOD-2 exhibit 46.6-fold and 21.5-fold ratiometric turn-ons, respectively. Moreover, unlike existing NIR NO donors, the photoNODs do not require encapsulation or multiphoton activation for use in live animals. In this study, we use PA tomography to monitor the local, irradiation-dependent release of NO from photoNOD-1 and photoNOD-2 in mice after subcutaneous treatment. In addition, we use a murine model for breast cancer to show that photoNOD-1 can selectively affect tumor growth rates in the presence of NIR light stimulation following systemic administration.

Graphical Abstract

[*]**Corresponding Author** jeffchan@illinois.edu.

[§]Author Contributions

E.Y.Z. and H.J.K. contributed equally.

Supporting Information

The Supporting Information is available free of charge on the ACS Publications website at DOI: 10.1021/jacs.8b05514.

Detailed materials, instrumentation, data processing methods and statistical analysis, tissue phantom preparation, pH stability, NO release quantification (UV–vis, EPR), mass spectrometry, cell culture information (including cytotoxicity and proliferation assays), PA spectra, in vivo PA turn-on data, TUNEL IHC, NMR data, and supplementary figures and tables (PDF)

The authors declare no competing financial interest.

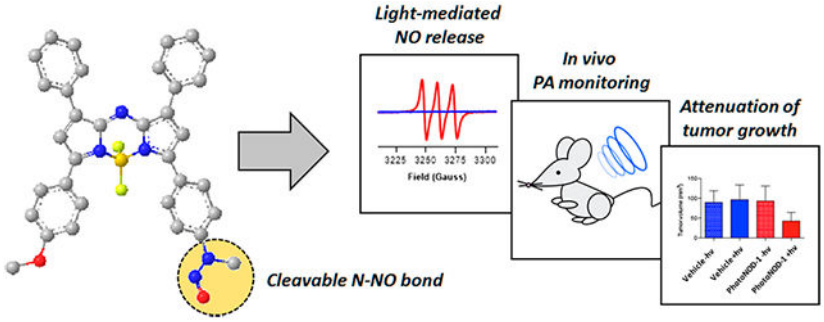

■ INTRODUCTION

Photoacoustic (PA) tomography is a noninvasive technology that combines the advantages of tissue-penetrant near-infrared (NIR) excitation with ultrasonic detection to achieve high-resolution imaging at depths of up to 10 cm in biological tissues.[1,2] These properties make PA imaging a powerful tool for live animal imaging relative to purely optical methods such as fluorescence imaging. While optical strategies have excellent utility for studies in cell culture and shallow tissues (≤1.5 mm), they suffer from poor resolution at greater depths due to the scattering of emitted light. Moreover, PA tomography has great translational potential, as it has already been employed for noninvasive, label-free studies of human subjects with breast cancer,[3] thyroid cancer,[4] inflammatory arthritis,[5] and scleroderma.[6] Several recent developments in small-molecule activatable PA sensors, or acoustogenic probes, have enabled the detection of metal ions,[7-9] hypoxia,[10,11] and nitric oxide (NO)[12,13] using PA readouts. However, the photochemical delivery of bioactive analytes (like NO) *in vivo* with PA monitoring is an underexplored area of research with great potential for the controlled modulation of biological processes.

Our recent progress toward *in vivo* detection of NO with PA tomography inspired our interest in developing NO-releasing molecules (NORMs) that can be activated by NIR light and generate a PA readout for real-time monitoring of delivery.[12] Light-mediated analyte release is uniquely powerful because it enables spatiotemporally controlled stimulation of a biological response. In particular, light in the NIR range is useful as an *in vivo* bioorthogonal trigger due to its low phototoxicity and enhanced tissue penetration relative to higher energy wavelengths.[14] The utility of NIR activation strategies has been demonstrated by a variety of recent studies in protein[15] and drug delivery,[16-22] photodynamic therapy,[17,21,23] carbon monoxide delivery,[24,25] antibody–drug conjugate activation,[26] gene expression,[27-29] and metal ion delivery.[30]

NO is an endogenously produced gasotransmitter that is important for vascular tone and neuronal signaling.[31] However, NO also has key roles in various other conditions, including inflammation,[32,33] infection,[34] reperfusion injury,[35] and cancer.[36,37] The role of NO is often studied in small-animal models by knocking out endogenous NO synthase (NOS) enzymes[38,39] or by systemic dosing of NOS inhibitors[39] or NO donors.[35,39,40] However, these strategies affect NO generation in a nonspecific manner and can alter normal NO signaling, potentially leading to incorrect conclusions. This has resulted in a growing interest

in NORMs that can be selectively activated in local regions or in response to specific stimuli to enable controlled, local modulation of NO levels without eliciting a global response.

To date, several classes of activatable NORMs have been developed with various release mechanisms and kinetics. NO release from these molecules can be triggered by pH, thermal activation, enzymatic activity, thiol-based transnitrosylation, or irradiation with light.[41] Photoactivatable NO-releasing molecules (photoNORMs) that incorporate iron, manganese, or ruthenium-nitrosyl moieties have been shown to release NO upon irradiation at wavelengths ranging from UV to NIR. However, these metal-nitrosyl donors commonly require encapsulation in nanodelivery systems to mitigate off-target NO release and toxicity.[42,43] Select examples of metal-nitrosyl complexes have been used in isolated tissues without encapsulation, but their toxicity has yet to be evaluated.[44-47] On the other hand, organic photoNORMs that typically offer greater stability in biological samples have also been developed. The first examples required the use of damaging UV irradiation to release NO from caged diazeniumdiolates,[48] aryl *N*-nitrosamines,[49] and nitrobenzenes.[50,51] Molecules stimulated by visible[52-56] and two-photon NIR light[57,58] were soon realized to improve tissue penetration and biocompatibility.

It was not until recently that visible light[59,60] and two-photon NIR-activated[61,62] photoNORMs were developed to incorporate a fluorescent readout following NO delivery. This enables calibration of the release based on the fluorescence signal, without the need for an additional NO detection method (e.g., NO-specific fluorescent dye or electrode). These have excellent potential as tools to study NO biology in cell culture due to their ability to elicit NO release in precise femtoliter volumes.[63] However, two-photon methods are limited to shallow tissue depths (1.5 mm),[64] and studies in cell culture do not accurately mimic the complex, three-dimensional network of cell types and biochemical signals found *in vivo.* This can generate discrepancies between cellular and animal studies. Therefore, it is critical to develop photoNORMs that can be used in native, deep-tissue contexts.[65]

Herein, we describe the synthesis and validation of NIR photoactivatable NO donors (photoNOD-1 and photoNOD-2) whose irradiation-based NO release can be monitored with PA tomography (Scheme 1). We characterize the NO release from these molecules and validate their chemostability and biocompatibility. Moreover, we illustrate the applicability of these first-in-class donors for NO release *in vivo* and demonstrate that selective irradiation of photoNOD-1 attenuates tumor growth in a murine model of breast carcinoma without affecting distal tissues.

■ RESULTS AND DISCUSSION

Design and Synthesis.

We hypothesized that the aza-BODIPY dye platform would be an ideal antenna for harvesting NIR light due to its large extinction coefficient ($>10^4$ M^{-1} cm^{-1}) at NIR wavelengths, which could provide sufficient energy to mediate N-nitroso bond cleavage.[54,56,66] This property also facilitates generation of strong PA signals upon excitation.[2] Moreover, the photophysical properties of aza-BODIPYs are known to be modulated by changes in chemical substitution, making this an ideal scaffold for ratiometric probe

generation.[10-12,67] photoNOD-1 and its water-soluble congener photoNOD-2 were designed with a photolabile alkylated *N*-nitroso moiety, which releases NO and an aza-BODIPY with a free aryl amine (rNOD-1 or rNOD-2) upon irradiation (Scheme 1). We hypothesized that the conversion of the electron-withdrawing *N*-nitroso bond to a more electron-rich N–H bond would cause a bathochromic shift in the absorbance maximum. Irradiation at both wavelengths would then generate two corresponding PA signals, enabling the simultaneous identification of photoNOD and rNOD.[10-12,67]

photoNOD-1 and photoNOD-2 were synthesized from 4′-aminoacetophenone (Scheme 2). Carbamate protection yielded **1**, which was alkylated with methyl iodide to afford the *N*-methylaniline trigger precursor. Next, this intermediate was subjected to Claisen–Schmidt condensation conditions with benzaldehyde, followed by Michael addition of nitromethane to yield **2a**. Dimerization with **3a** in the presence of ammonium acetate yielded aza-dipyrromethene **4a**. Alternatively, deprotection of **2a** with trifluoroacetic acid to afford **2b** followed by dimerization with **3b**[12] yielded compound **4b**. Boron chelation in the presence of triethylamine and boron trifluoride diethyl etherate yielded rNOD-1 and aza-BODIPY **5**. Copper-catalyzed click chemistry was utilized to install the tetramethylammonium PEG solubilizing group **6**[12] onto aza-BODIPY **5**, forming rNOD-2. Nitrosation of rNOD-1 and rNOD-2 with sodium nitrite in acetic acid yielded photoNOD-1 and photoNOD-2, respectively.

In Vitro Characterization of photoNODs.

Because the PA signal is proportional to molar absorptivity, the relative PA intensity of a molecule can be conveniently approximated by its absorbance spectrum at any given wavelength.[68] Absorbance spectra were acquired for each compound in chloroform and aqueous buffer with additives to enable solubilization (50% ethanol for photoNOD-1, Figure 1a; 0.1% Cremophor EL (CrEL) for photoNOD-2, Figure 1b; full spectra may be found in Figure S1). As hypothesized, the photoNODs exhibit absorbance maxima near 680 nm (λ_{blue}), while the rNODs are red-shifted to wavelengths greater than 730 nm (λ_{red}). All four species maintain absorptions in the first biological imaging window with extinction coefficients in the expected range (Tables 1 and S1). Importantly, these absorbance maxima lie within the wavelength range of commercial PA tomographers (typically 680–950 nm).[11]

To assess the ability of NIR irradiation to penetrate through tissue and activate the photoNODs, a solution of each compound was placed within a tissue-mimicking phantom (depth of ~1 cm) that can scatter incident light to evenly illuminate the sample. These solutions were irradiated for up to 40 min using a PA tomographer, and the change in ratiometric PA signal was monitored over time (Figure 1c,d). Formation of the rNODs was apparent after 5 min of irradiation, and maximal release was noted after 30–40 min of irradiation (Figure 1c-e). Absorbance spectra of the irradiated solutions were then acquired, and spectral analysis revealed that approximately 54% of photoNOD-1 and 88% of photoNOD-2 were consumed, corresponding to 5.4 and 8.8 μM NO, respectively (Figure S2; calculations based on measured extinction coefficients, Table S1). Further irradiation beyond this point did not increase the yield of NO. The identity of the rNODs was further confirmed with high-resolution mass spectrometry (Figures S3-S8).

We then sought to confirm that NO is the species released by electron paramagnetic resonance (EPR) spectroscopy. Deoxygenated solutions of each photoNOD (200 μM in water containing 50% DMF) were irradiated at λ_{blue} (Figure S9) in the presence of $Fe(MGD)_2$, a known NO spin-trap. Upon nitrosylation, $Fe(MGD)_2$ generates a diagnostic triplet (g = 2.04) corresponding to the MGD-Fe-NO complex (Figure 2a,b) as well as an apparent color change consistent with the generation of rNODs (Figure 2c). Importantly, because only NO (and not NO^+) can react with $Fe(MGD)_2$ to generate an EPR-active species,[51,69,70] this confirmed that irradiation induces denitrosylation of both photoNODs. NO release was then quantified by EPR after 5 or 40 min of irradiation to confirm that release can be controlled by irradiation time. photoNOD-1 released 20.4 μM (10%) NO after 5 min and 30.1 μM (15%) after 40 min, and photoNOD-2 released 38.7 μM (20%) NO after 5 min and 73.9 μM (37%) NO after 40 min (Figures 2d and S10). We attribute the difference in release efficiencies to solubility-dependent changes in the photophysical properties rather than intrinsic differences.

To evaluate chemostability, each photoNOD was incubated with reduced glutathione, copper(I), copper(II), iron(II), and iron(III) to survey the effect of these species toward transnitrosylation, denitrosylation, or denitrosation. The absorbance spectra of these solutions were then acquired, and the ratiometric fold turn-on was calculated. However, no significant ratiometric turn-on was detected in the presence of any of these species (Figures 3a,b and S11). Next, the photoNODs were incubated in human plasma to evaluate stability during circulation, and again no ratiometric turn-on was observed. Finally, we sought to ensure that the photoNODs are stable to cytochrome P450 (CYP450) enzymes. CYP450s are known to oxidize some *N*-alkyl-*N*-nitrosamines to α-hydroxy-*N*-nitrosamine intermediates, which can form DNA-alkylating diazonium species.[71] We incubated the photoNODs with NADPH-supplemented rat liver microsomes, a source of CYP450s, and verified that these conditions did not generate a ratiometric turn-on, suggesting that the photoNODs are not substrates for these enzymes. This is an especially important finding because *N*-nitrosamines are often considered untenable for biological studies based upon the assumption that they are carcinogenic.[71-74] In contrast, solutions of photoNOD-1 subjected to 5 min of irradiation at λ_{blue} yielded a 46.6-fold turn-on (theoretical maximum of 115.4-fold calculated for rNOD-1, 40.4%, Figure 3a), while photoNOD-2 yielded a 21.5-fold ratiometric turn-on (theoretical maximum of 45.4-fold for rNOD-2, 47.4%, Figure 3b), indicating robust and selective turnover of the photoNODs following irradiation. Additionally, the absorbance properties of the photoNODs proved to be independent of pH in the range of 4.0–10.0, indicating that NO could be reliably released by irradiation at λ_{blue} regardless of pH (Figure S12). Collectively, these data indicate that irradiation at λ_{blue} generates the rNODs with concomitant release of NO, and this process can be conveniently monitored by ratiometric absorbance or PA imaging. The apparent stability of the photoNODs, in conjunction with the turnover response following irradiation, suggests that the photoNODs should be applicable for controlled NO release in living systems.

We next surveyed the effect of the photoNODs and rNODs on the viability of live cells to evaluate their biocompatibility for *in vivo* applications. HEK293T cells were treated with photoNODs and rNODs (30 μM) for 24 h. The toxicity was evaluated by fluorescence microscopy using Hoechst and propidium iodide counterstaining.[75,76] All compounds that

were tested were noncytotoxic under these conditions, maintaining greater than 95% cell viability (Figure S13).

Characterization of photoNODs *in Vivo*.

Having established stability and cellular compatibility, we sought to characterize the photoNODs and rNODs in live animals. Each compound was subcutaneously administered into the flank of a BALB/c mouse, and PA spectra from 680 to 850 nm were acquired (Figure 4a,d). From these data, the optimal wavelengths for *in vivo* irradiation/excitation, λ_{PAblue} and λ_{PAred}, were determined (700 and 830 nm for photoNOD-1 and rNOD-1; 710 and 810 nm for photoNOD-2 and rNOD-2). These wavelengths were selected to maximize the ratiometric signal (Figure 4a,d).

To validate the irradiation-mediated release of NO in vivo, each photoNOD was administered subcutaneously into both flanks of BALB/c mice, and the ratiometric turn-on was monitored with and without 5 min of irradiation at λ_{PAblue} (Figure 4c,f). This time point was selected to enable fast and convenient experiments while also sustaining significant NO release (as described in our *in vitro* characterization). *In vivo* irradiation of photoNOD-1 yielded a 1.37-fold ratiometric turn-on (theoretical maximum of 2.09-fold, 65.6% release), with a 1.12-fold turn-on in the absence of irradiation (Figure 4b). photoNOD-2 yielded a 2.29-fold ratiometric turn-on (theoretical maximum turn-on of 2.60-fold, 88.1% release), while only a 1.27-fold turn-on was observed in the absence of irradiation (Figure 4e). Of note, the values obtained for the controls without irradiation are not statistically different from values obtained for a vehicle control. These results encouraged the application of photoNODs modulate biology within small-animal models.

Modulation of Tumor Progression with photoNOD-1.

The key advantage of using a photocontrollable NO donor over a standard NORM is the ability to release NO with high spatiotemporal control. This enables systemic administration of photoNORMs while preventing off-target side effects outside of the tissue area of interest. After establishing that the photoNODs were capable of selectively releasing NO upon irradiation, we sought to demonstrate the capability of this system for local release following systemic administration in a proof-of-principle study. NO has been implicated for its toxicity to cancer cells at high concentrations, and various NO donors have been demonstrated to be effective for inhibiting tumor growth *in vivo*.[77-80] Moreover, it has been shown that the administration of NO can sensitize hypoxic tumors to both chemo- and radiotherapy.[81-91] Thus, we hypothesized that an *in vivo* tumor model could serve as an effective system to demonstrate controlled NO release using the photoNODs.

For our initial studies, we selected photoNOD-2 for *in vivo* administration based on its water solubility and resulting superior PA signal. Unfortunately, when photoNOD-2 was administered systemically via retroorbital injection,[92] no apparent signs of tumor uptake were observed via PA imaging. We hypothesized that this charged molecule was likely undergoing rapid clearance,[93,94] and therefore we repeated the study with the more lipophilic photoNOD-1. Indeed, PA imaging at 4 h following administration revealed a substantial increase in the ratiometric PA signal ($\lambda_{\text{PAblue}}/\lambda_{\text{APAred}}$) for photoNOD-1 when

compared to photoNOD-2 and a vehicle control, corresponding to uptake (Figure S14). For this reason, we chose to employ photoNOD-1 for experiments requiring systemic administration. We posit that photoNOD-2 would be superior for experiments in which local administration with temporal control of NO release is required.

Inspired by various reports suggesting the ability of NO to manipulate tumor growth, and our own preliminary studies suggesting that NO can decrease proliferation of cultured 4T1 cells (Figure S15), we sought to assess the physiological impact of selective light-mediated NO release. To this end, 4T1 tumors were implanted in both flanks of BALB/c mice. At 5 days post-implantation, mice were randomly divided into control and treatment groups. Either photoNOD-1 or vehicle was administered systemically. Four hours post-injection, the left tumor was irradiated at λ_{PAblue} (700 nm) for 5 min while the right tumor was not (Figure 5a). Release was monitored by PA imaging before and after irradiation (left tumor) or a 5 min period without irradiation (right tumor) (Figure 5b,c). A ratiometric turn-on response was observed selectively in the irradiated tumors of the treatment group, corresponding to the formation of rNOD-1 and NO release (Figures 5c and S16). This process was repeated every other day for a total of 7 days (4 doses). Over the course of the experiment, tumor volumes were measured using calipers, the mice were weighed, and their behavior was monitored (e.g., signs of pain and distress).[95] One week following the initial treatment, we observed that the average tumor volumes for vehicle-treated (with and without irradiation) and photoNOD-1-treated (without irradiation) tumors were approximately 90 mm^3. In contrast, the average volume for irradiated tumors in photoNOD-1-treated mice was only 42 mm^3 (Figure 5d). The difference in tumor volume between the treated mice and each control group was greater than 50% (Figure 5e), indicating that NO release was modulating tumor progression via NO-induced cytotoxicity or suppression of proliferation.[96-98] To further confirm these results, we excised tumor tissue following treatment and performed histological staining for apoptotic cells. We found that the number of apoptotic cells was greater following irradiation as compared to the control, indicating that tumor growth suppression was likely occurring via NO-induced apoptosis (Figure S17). Of note, we also confirmed that photoNOD-1 and rNOD-1 are nontoxic to 4T1 cells even at elevated concentrations (Figure S18).

Importantly, mice treated with photoNOD-1 experienced no significant weight loss (Figure 6b) or behavioral changes during this experiment. To determine the localization of photoNOD-1 in various tissue types, tumor-bearing mice were sacrificed 4 h following administration, and *ex vivo* PA images of various organs were acquired. A trend of increased PA signal at λ_{PAblue} was observed in the heart, liver, kidneys, spleen, and tumor tissue of treated mice as compared to the vehicle control (Figure 6a and c), possibly corresponding to photoNOD-1 uptake. The uptake of photoNOD-1 in a variety of tissues is advantageous, because it suggests that NO release from photoNOD-1 could be selectively targeted to different organs by local irradiation for a breadth of applications. Overall, these experiments confirmed that NO release from photoNOD-1 is limited to the area of irradiation, demonstrating that it can be used for NO delivery with high spatiotemporal control.

■ CONCLUSION

The photoNODs represent the first small-molecule analyte donors that incorporate a direct PA readout to enable noninvasive monitoring of analyte release in live animals. Existing PA-compatible analyte carriers (e.g., carbon nanotubes, gold nanoparticles, and porphysomes)[99] that simply track analyte distribution do not undergo an intrinsic PA signal change upon release and cannot provide reliable confirmation of delivery.[100-105] On the other hand, organic nanoparticles, microsomes, and liposomes that are coloaded with an analyte donor and responsive PA sensor can detect analyte flux; however, these constructs are not ideal because they indirectly couple analyte release to the PA response.[106,107] Small-molecule-based donors such as the photoNODs overcome these limitations because each state (pre- and post-release) has a different PA signature, allowing for facile identification of each. This unique feature, coupled with the noninvasiveness and high resolution of PA imaging, mitigates the need for invasive procedures (e.g., analyte-specific electrode), additional contrast agents, or *ex vivo* analyses to confirm analyte delivery. Furthermore, the PA readouts of the photoNODs make them superior for *in vivo* applications as compared to existing fluorescence-based photoNORMs,[62,66,108] which are optimal for applications in cells and in shallow tissues due to the depth-dependent attenuation of light in tissue.

When designing the photoNODs, it was essential to strike a balance between chemostability and light-based lability of the *N*-nitroso bond. Our *in vitro* analysis demonstrates that both photoNODs are stable unless activated by light, including in the presence of CYP450 enzymes, alleviating potential concerns of formation of potent alkylating agents. Additionally, the rNODs generated by irradiation were designed to be weakly nucleophilic and hence less susceptible to back-capture of released NO, unlike nitrosation-based probes for NO that feature electron-rich aniline triggers.[12,109] PA imaging following systemic injection demonstrated that photoNOD-1 was superior to photoNOD-2 in terms of distribution and tissue accumulation. However, photoNOD-2 presents good PA properties following local administration. This phenomenon highlights the utility of noninvasive PA monitoring, because evaluation of compound accumulation would otherwise require the sacrifice of multiple animals and subsequent tissue analysis at various time points. Finally, photoNOD-1 can be selectively activated in a tissue of interest following systemic administration without causing the global effects that would be expected for standard NORMs.

We envision that slight modifications to the photoNOD scaffold, such as incorporating tumor- or tissue-targeting motifs, could significantly increase uptake, dosage, and specificity. More broadly, the development of small molecule donors that can be activated to modulate biological processes with a deep-tissue compatible PA readout provides an exciting avenue for validating cellular findings in the native biological context. While our work in this study focuses on the delivery of NO, this design strategy may be generalizable to other analytes, broadening the scope of synergistic NIR photorelease and PA imaging.

■ EXPERIMENTAL DETAILS

Synthetic Methods.

tert-Butyl (4-Acetylphenyl)carbamate (1).—To a 250 mL round-bottomed flask (RBF) were added 4′-aminoacetophenone (6.7 g, 50 mmol, 1.0 equiv) and di-*tert*-butyl dicarbonate (13.1 g, 60 mmol, 1.2 equiv). The reaction vessel was capped and flushed with nitrogen. 1,4-Dioxane (60 mL) was added, and the solution was heated to 100 °C for 8.5 h. The reaction was cooled and concentrated to an oil that crystallized to a solid. The solid was washed with 1:3 v/v EtOAc/hexanes to give one batch of pure product. The filtrate was then concentrated to a solid and washed with 1:4 EtOAc/hexanes to afford a second batch of pure product (total: 10.1 g, 43 mmol, 86% yield). ^{1}H NMR (400 MHz, $CDCl_3$) δ 7.89 (d, J = 8.4 Hz, 2H), 7.46 (d, J = 8.3 Hz, 2H), 2.55 (s, 3H), 1.50 (s, 9H). ^{13}C NMR (125 MHz, $CDCl_3$) δ 197.13, 152.35, 143.15, 131.84, 129.94, 117.53, 81.35, 28.37, 26.49.

tert-Butyl Methyl (4-(4-Nitro-3-phenylbutanoyl)phenyl)-carbamate (2a).—To a 250 mL RBF were added **1** (3.0 g, 12.8 mmol, 1.0 equiv) and anhydrous THF (40 mL) under nitrogen. The reaction mixture was cooled to 0 °C, and sodium hydride (60 wt % dispersion in mineral oil) (0.61 g, 15.3 mmol, 1.2 equiv) was added portion-wise over the course of 10 min. After 20 min, methyl iodide (1.57 mL, 31.9 mmol, 2.5 equiv) was added, and the white suspension was warmed to room temperature and stirred until it formed an amber solution. After 40 min at this temperature, completion was noted by TLC (3:17 v/v EtOAc/hexanes); the reaction mixture was concentrated, and the crude residue was taken up in EtOAc and washed with brine (3x). The organic layer was dried over sodium sulfate and concentrated to a yellow oil (quantitative yield). A portion was transferred to a 50 mL RBF (0.59 g, 2.38 mmol, 1.0 equiv) and stirred with benzaldehyde (0.27 mL, 2.62 mmol, 1.1 equiv), potassium hydroxide (10 M, 0.72 mL, 7.15 mmol, 3.0 equiv), and ethanol (10 mL) for 2.5 h. Nitromethane (1.90 mL, 35.7 mmol, 15 equiv) was added, and the solution was stirred at room temperature for 10.5 h, fully converting to a brown solution. The reaction was concentrated, diluted with brine, and extracted with dichloromethane. The organic layers were dried over sodium sulfate, filtered, and concentrated. The product was purified via silica column chromatography in 1:4 v/v EtOAc/hexanes to afford a yellow oil (0.47 g, 1.4 mmol, 59% yield over three steps). ^{1}H NMR (500 MHz, CDO3) δ 7.88 (d, J = 8.8 Hz, 2H), 7.36 (d, J = 8.8 Hz, 2H), 7.34–7.31 (m, 2H), 7.30–7.26 (m, 3H), 4.83 (dd, J = 12.5, 6.5 Hz, 1H), 4.68 (dd, J = 12.5, 8.1 Hz, 1H), 4.22 (p, J = 7.1 Hz, 1H), 3.48–3.35 (m, 3H), 3.30 (s, 3H), 1.48 (s, 9H). ^{13}C NMR (125 MHz, $CDCl_3$) δ 195.85, 154.10, 148.59, 139.24, 132.57, 129.19, 129.16, 128.68, 127.99, 127.57, 124.44, 81.44, 79.69, 41.48, 39.44, 36.90, 28.40, 14.33.

tert-Butyl (Z)-(4-(5-((5-(4-Methoxyphenyl)-3-phenyl-2H-pyrrol-2-ylidene)amino)-4-phenyl-1H-pyrrol-2-yl)phenyl)(methyl)-carbamate (4a).—To a 50 mL RBF were added **2a** (475 mg, 1.2 mmol, 1.0 equiv), **3a**[12] (718 mg, 2.4 mmol, 2.0 equiv), and ethanol (36 mL), and the mixture was stirred at 60 °C until completely dissolved. Ammonium acetate (1.38 g, 18 mmol, 15 equiv) was added, and the reaction was refluxed for 15 h. The solution was then cooled to room temperature; the solids were isolated by filtration and purified by gradient silica column chromatography (dichloromethane, then

1:199 v/v methanol/dichloromethane) to yield a blue-green solid (185 mg, 0.30 mmol, 25%). ^{1}H NMR (500 MHz, $CDCl_3$) δ 8.02–7.92 (m, 4H), 7.79 (d, J = 8.3 Hz, 2H), 7.67 (d, J = 8.1 Hz, 2H), 7.40–7.29 (m, 9H), 7.06 (s, 1H), 6.96 (s, 1H), 6.91 (d, J = 8.3 Hz, 2H), 3.81 (s, 3H), 3.30 (s, 3H), 1.54 (s, 9H). ^{13}C NMR (125 MHz, $CDCl_3$) δ 161.74, 159.90, 154.46, 153.35, 148.00, 145.76, 144.53, 144.45, 139.09, 134.10, 133.60, 130.34, 129.15, 129.05, 128.94, 128.74, 128.38, 128.18, 128.15, 127.98, 127.81, 127.50, 125.98, 125.32, 125.07, 116.92, 114.53, 113.86, 112.02, 80.85, 53.54, 37.07, 28.45.

(Z)-N-Methyl-4-(4-phenyl-5-((3-phenyl-5-(4-(prop-2-yn-1-yloxy)-phenyl)-2H-pyrrol-2-ylidene)amino)-1H-pyrrol-2-yl)aniline (4b).—To a 25 mL RBF were added **2a** (1.13g, 2.84 mmol, 1.0 equiv), trifluoroacetic acid (2 mL), and dichloromethane (10 mL), and this was stirred for 1 h at room temperature. Upon completion by TLC, the reaction mixture was cooled to 0 °C and quenched with saturated sodium bicarbonate (5 mL) followed by slow addition of solid sodium carbonate until gas evolution ceased. The reaction mixture was extracted with dichloromethane, dried over sodium sulfate, filtered, and concentrated to afford a clear oil, **2b**, which was used without purification (0.60 g, 2.52 mmol, 89% yield). A portion (0.2 g, 0.84 mmol, 1.0 equiv) was added to a 50 mL RBF; **3b**[12] (0.54 g, 1.69 mmol, 2.0 equiv) and *n*-butanol (20 mL) were added and warmed at 110 °C until solids completely dissolved. Ammonium acetate (0.97 g, 12.6 mmol, 15 equiv) was added, and the reaction was stirred at this temperature for 8 h. The solution was concentrated via rotary evaporation, diluted with brine, and extracted with EtOAc. The organic layer was dried over sodium sulfate, filtered, and concentrated. The product was purified via silica column chromatography (4:1 v/v dichloromethane/hexanes with 0.1% Et_3N) to afford a blue-green solid (0.150 g, 0.28 mmol, 33% yield). ^{1}H NMR (400 MHz, $CDCl_3$) δ 8.07 (dt, J = 8.0, 1.8 Hz, 5H), 7.92 (d, J = 8.6 Hz, 2H), 7.82–7.77 (m, 2H), 7.46–7.27 (m, 6H), 7.13–7.09 (m, 2H), 7.00 (s, 1H), 6.72 (d, J = 8.7 Hz, 2H), 4.79 (d, J = 2.4 Hz, 2H), 4.28 (d, J = 5.4 Hz, 1H), 2.97 (d, J = 5.2 Hz, 3H), 2.59 (t, J = 2.4 Hz, 1H). ^{13}C NMR (126 MHz, $CDCl_3$) δ 162.43, 158.12, 155.00, 151.68, 145.52, 145.29, 144.14, 137.30, 134.45, 133.73, 129.32, 129.16, 128.78, 128.16, 128.14, 128.00, 127.21, 126.99, 125.78, 121.39, 118.05, 115.57, 112.41, 110.40, 78.28, 75.88, 55.95, 29.70.

rNOD-1.—To a 100 mL RBF were added **4a** (100 mg, 0.166 mmol, 1.0 equiv), dichloromethane (10 mL), and Et_3N (0.33 mL, 2.48 mmol, 15 equiv). Boron trifluoride diethyl etherate (0.30 mL, 2.48 mmol, 15 equiv) was added dropwise. The reaction was stirred for 6 h before additional Et_3N (0.33 mL, 2.48 mmol, 15 equiv) and boron trifluoride diethyl etherate (0.30 mL, 2.48 mmol, 15 equiv) were added. The reaction was stirred for another 15 h. The reaction mixture was diluted with dichloromethane, washed with a saturated solution of sodium bicarbonate, and dried over sodium sulfate. The crude product was purified via silica column chromatography using a gradient from 1:2 v/v EtOAc/hexanes to 1:1 v/v EtOAc/hexanes to afford a red-brown solid (72.7 mg, 0.131 mmol, 79% yield). ^{1}H NMR (500 MHz, $CDCl_3$) δ 8.14 (d, J = 8.9 Hz, 2H), 8.11–8.02 (m, 6H), 7.50–7.34 (m, 6H), 7.18 (s, 1H), 7.01 (d, J = 8.8 Hz, 2H), 6.95 (s, 1H), 6.70–6.60 (m, 2H), 3.88 (s, 3H), 2.93 (s, 3H). ^{13}C NMR (125 MHz, $CDCl_3$) δ 161.19, 160.12, 154.34, 152.40, 146.61, 144.02, 143.70, 140.21, 133.35, 132.79 (t, J = 5.5 Hz), 132.52, 131.26 (t, J = 4.6 Hz), 129.45, 129.36, 129.18, 128.63, 128.61, 128.58, 125.25, 119.67, 119.38, 117.30, 114.18, 112.38,

55.51, 30.23. ^{19}F NMR (470 MHz, CDO3) δ −132.68 (dd, J = 64.8, 32.3 Hz). ^{11}B NMR (161 MHz, $CDCl_3$) δ 1.27 (t, J = 32.4 Hz).

4-(5,5-Difluoro-1,9-diphenyl-7-(4-(prop-2-yn-1-yloxy)phenyl)-5H-5l4,6l4-dipyrrolo[1,2-c:2′,1′-f][1,3,5,2]triazaborinin-3-yl)-N-methylaniline (5).—To a 50 mL RBF were added **4b** (0.15 g, 0.28 mmol, 1 equiv), dichloromethane (11.3 mL), Et_3N (4.9 mL, 28 mmol, 100 equiv), and boron trifluoride diethyl etherate (5.2 mL, 43 mmol, 150 equiv) under nitrogen at 0 °C, and this was stirred for 2.5 h at room temperature. Additional boron trifluoride diethyl etherate (5.2 mL, 43 mmol, 150 equiv) was added at 0 °C, and the reaction was stirred at room temperature for 21 h. The reaction mixture was diluted with dichloromethane, washed with a saturated solution of sodium bicarbonate, and dried over sodium sulfate. The crude product was purified via silica column chromatography in 1:2 v/v EtOAc/hexanes to afford a red-brown solid (0.14 g, 0.23 mmol, 82% yield). ^{1}H NMR (500 MHz, $CDCl_3$) δ 8.15–8.10 (m, 2H), 8.06 (dt, J = 8.3, 6.0 Hz, 6H), 7.50–7.39 (m, 5H), 7.37 (t, J = 7.3 Hz, 1H), 7.18 (d, J = 3.6 Hz, 1H), 7.10–7.05 (m, 2H), 6.93 (s, 1H), 6.63 (t, J = 8.0 Hz, 2H), 4.75 (t, J = 2.2 Hz, 2H), 2.93–2.82 (m, 3H), 2.56 (t, J = 2.4 Hz, 1H). ^{13}C NMR (125 MHz, $CDCl_3$) δ 160.68, 159.05, 153.28, 152.74, 146.99, 143.92, 143.75, 139.59, 133.52, 133.11, 132.46, 131.23, 129.58, 129.54, 129.23, 128.72, 128.70, 128.63, 126.36, 120.15, 119.01, 117.12, 115.05, 112.49, 78.57, 76.14, 56.08, 30.18. ^{19}F NMR (471 MHz, $CDCl_3$) δ −132.29 (dd, J = 61.2, 32.6 Hz). ^{11}B NMR (128 MHz, $CDCl_3$) δ 1.31 (t, J = 32.3 Hz).

rNOD-2.—To a two-neck 25 mL RBF were added **5** (0.05 g, 0.086 mmol, 1 equiv), **6**[12] (0.12 g, 0.3 mmol, 3.5 equiv), copper sulfate pentahydrate (0.1 g, 0.43 mmol, 5 equiv), and tris-hydroxypropyl-triazolylmethylamine (7 mg, 0.02 mmol, 0.2 equiv), and this was flushed under nitrogen for 1 h. (+)-Sodium L-ascorbate (0.025 g, 0.129 mmol, 1.5 equiv) was added along with degassed THF (4.5 mL) and degassed water (1.5 mL). The reaction was stirred for 21 h at room temperature, diluted with dichloromethane, and washed with brine. The aqueous layer was further extracted with a mixture of dichloromethane and isopropanol (2:1 v/v). The combined organic layers were dried over sodium sulfate, filtered, and concentrated. The crude product was loaded onto Celite and purified via neutral alumina column chromatography in 1:19 v/v MeOH/dichloromethane (2x) to afford a red-brown solid (0.025 g, 0.028 mmol, 33% yield). ^{1}H NMR (500 MHz, CD_2Cl_2) δ 8.14 (d, J = 8.7 Hz, 2H), 8.09 (d, J = 7.4 Hz, 2H), 8.05 (d, J = 7.7 Hz, 2H), 8.02–7.95 (m, 3H), 7.45 (dt, J = 21.2, 7.5 Hz, 5H), 7.38–7.30 (m, 2H), 7.29–7.24 (m, 1H), 7.12 (d, J = 8.4 Hz, 2H), 6.91–6.83 (m, 3H), 5.25 (s, 2H), 4.54 (t, J = 4.8 Hz, 2H), 3.85 (t, J = 4.9 Hz, 2H), 3.68 (bs, 2H), 3.58–3.45 (m, 10H), 3.12 (s, 9H), 2.91 (d, J = 5.0 Hz, 3H). ^{13}C NMR (125 MHz, CD_2Cl_2) δ 161.42, 159.85, 154.97, 151.13, 147.83, 144.40, 143.82, 143.14, 138.04, 133.99, 133.84, 132.57, 131.42, 130.03, 129.79, 129.29, 129.07, 129.00, 128.70, 126.85, 125.05, 121.14, 117.67, 116.63, 115.20, 113.00, 70.97, 70.75, 70.74, 70.56, 69.66, 65.93, 65.37, 62.49, 54.75, 50.86, 29.99. ^{19}F NMR (471 MHz, CD_2Cl_2) δ −131.65 (dd, J = 65.5, 31.7 Hz). ^{11}B NMR (128 MHz, CD_2Cl_2) δ 1.25 (t, J = 32.5 Hz).

photoNOD-1.—To a 25 mL RBF were added rNOD-1 (72.7 mg, 0.130 mmol, 1.0 equiv), THF (8.7 mL), dichloromethane (4.35 mL), acetic acid (4.35 mL), and sodium nitrite (44.8

mg, 0.653 mmol, 5.0 equiv). The reaction mixture was stirred for 2 h at room temperature. Upon completion by TLC, the reaction was diluted in dichloromethane and quenched with a saturated solution of sodium bicarbonate. The organic layer was dried, concentrated, and purified by silica column chromatography in 4:1 v/v dichloromethane/hexanes to yield a green solid (36.9 mg, 0.63 mmol, 48% yield). ^{1}H NMR (500 MHz, $CDCl_3$) δ 8.17 (d, J = 8.5 Hz, 2H), 8.14 (d, J = 8.7 Hz, 2H), 8.10–8.04 (m, 4H), 7.69 (d, J = 8.4 Hz, 2H), 7.45 (h, J = 7.0, 6.5 Hz, 6H), 7.12 (s, 1H), 7.03 (s, 2H), 7.01 (s, 1H), 3.89 (s, 3H), 3.48 (s, 3H). ^{13}C NMR (125 MHz $CDCl_3$) δ 162.62, 160.68, 155.17, 146.45, 144.84, 144.71, 143.33, 142.44, 132.57, 132.10 (t, J = 4.9 Hz), 132.03, 130.75 (t, J = 4.5 Hz), 130.68, 129.71, 129.42, 129.24, 129.20, 128.64, 128.61, 123.52, 119.66 (d, J = 3.6 Hz), 118.30, 118.01 (d, J = 4.1 Hz), 114.44, 55.51, 30.65. ^{19}F NMR (471 MHz, $CDCl_3$) δ −131.97 (dd, J = 63.5, 31.7 Hz). ^{11}B NMR (161 MHz, CDO3) δ 1.08 (t, J = 31.7 Hz).

photoNOD-2.—To a 25 mL RBF were added rNOD-2 (0.014 g 0.015 mmol, 1 equiv), acetic acid (0.51 mL), THF (1 mL), and dichloromethane (1 mL), and this was cooled to 0 °C. Sodium nitrite (5 mg, 0.0772 mmol, 5 equiv) was added and stirred for 1 h. The reaction was diluted in dichloromethane and washed with saturated sodium bicarbonate. The compound was extracted from the aqueous layer using dichloromethane/isopropanol (2:1 v/v) and washed with brine. The organic layer was dried over sodium sulfate and concentrated. The product was purified via neutral alumina column chromatography in 1:19 v/v MeOH/dichloromethane to afford a blue solid (0.009 g, 0.01 mmol, 66% yield). ^{1}H NMR (500 MHz, CD_2Cl_2) δ 8.18 (d, J = 8.9 Hz, 2H), 8.16 (d, J = 9.0 Hz, 2H), 8.09 (ddt, J = 9.6, 6.4, 1.5 Hz, 4H), 8.02 (s, 1H), 7.74–7.71 (m, 2H), 7.52–7.42 (m, 6H), 7.20 (d, J = 1.1 Hz, 1H), 7.19–7.16 (m, 2H), 7.09 (d, J = 1.2 Hz, 1H), 5.30 (s, 2H), 4.58 (dd, J = 5.6, 4.6 Hz, 2H), 3.89 (dd, J = 5.6, 4.7 Hz, 2H), 3.85 (td, J = 5.0, 2.8 Hz, 2H), 3.82–3.77 (m, 2H), 3.61–3.55 (m, 4H), 3.55–3.51 (m, 4H), 3.48 (s, 3H), 3.31 (s, 9H). ^{13}C NMR (125 MHz, CD_2Cl_2) δ 161.93, 160.87, 156.01, 146.95, 145.35, 144.14, 143.46, 143.18, 133.00, 132.68, 132.51, 131.28, 131.08, 130.36, 129.94, 129.89, 129.76, 129.23, 129.20, 125.10, 124.52, 120.42, 118.92, 115.68, 71.09, 70.87, 70.79, 70.77, 69.82, 66.00, 65.66, 62.67, 54.87, 50.90, 31.25. ^{19}F NMR (471 MHz, CD2Q2) δ −131.31 (dd, J = 63.7, 31.8 Hz). ^{11}B NMR (161 MHz, CD_2Cl_2) δ 1.23, 1.04, 0.83. ^{11}B NMR (161 MHz, CD_2Cl_2) δ 1.03 (t, J = 32.0 Hz).

In Vitro Irradiation.

A solution of photoNOD-1 or −2 (10 μM in chloroform) was prepared, and initial absorbance spectra were obtained (400 to 900 nm). Solutions (400 μL) were pipetted into FEP tubing (0.08 in. diameter, cut to 5 cm long), and the tubing was inserted into the tissue phantom (see Supporting Information) and sealed by folding over the ends and securing with additional tubing (0.12 in. diameter). Initial PA measurements were acquired at 680 and 730 nm (photoNOD-1) or 680 and 750 nm (photoNOD-2) (continuous mode, 6 s rotation time). Following the initial measurement, subsequent PA irradiations at 680 nm were conducted for a total scan time of 0.5–40 min (continuous mode with 6 s rotation time for 0.5 and 1 min; step-and-shoot mode (120 angles, 41 pulses per angle) for longer time points), and PA images were acquired at both wavelengths after each time point. After the 40 min time point, the solution was removed from the FEP tubing, and absorbance spectra were obtained (400–900 nm). Control PA measurements were acquired after periods of 0.5–40 min of darkness

(using fresh samples of photoNOD-1 or −2 for each time point) to assess turnover in the absence of irradiation. Each time point was performed in triplicate.

Stability Assays.

Reported concentrations for these studies describe the final concentration after addition of all species. photoNOD-1 (5 μM) was preincubated for >10 min at 37 °C in 20 mM HEPES buffer with 50% EtOH (pH 7.4) before incubation with GSH (1 mM), $[(CH_3CN)_4Cu]PF_6$ (20 μM), $CuCl_2$ (20 μM), $FeSO_4{\cdot}7H_2O$ (20 μM), $FeCl_3$ (20 μM). photoNOD-1 was also incubated in rat liver microsomes (10 μL/mL) with NADPH (5 μM), and in human plasma (20% by volume) in PBS. Immediately after addition, initial absorbance spectra were acquired (400–900 nm). After 1 h, final absorbance spectra were acquired. Stability was plotted by determining the ratio of absorbance at λ_{red} to absorbance at λ_{blue} before and after incubation. All experiments were performed in triplicate. Note that Cu(I) and Fe(II) experiments were carried out using degassed solutions under nitrogen atmosphere. The same experiments were carried out for photoNOD-2 in 20 mM HEPES buffer with 0.1% CrEL (pH 7.4). CYP450 activity was validated prior to this analysis with *N*-nitroso-*N*-methylaniline (NMA), a known substrate of CYP450s found in rat liver microsomes. Rat liver microsomes (10 μM) were incubated with 100 μM NMA and 500 μM NADPH in 100 mM potassium phosphate buffer, pH 7.4. After 1.5 h of vigorous shaking at 30 °C and extraction with ethyl acetate, full consumption of NMA was observed by TLC.

For comparison, solutions of photoNOD-1 (5 μM) in 20 mM HEPES buffer with 50% EtOH and photoNOD-2 (5 μM) in 20 mM HEPES buffer with 0.1% CrEL were prepared. Solutions were irradiated (photoNOD-1, 680 nm; photoNOD-2, 690 nm) in FEP tubes in tissue-mimicking phantoms as previously described (see In Vitro Irradiation). Absorbance spectra were obtained before and after irradiation to determine ratiometric turn-on.

EPR Analysis of photoNOD NO Release.

The Fe(II) complex with *N*-(dithiocarbamoyl)-*N*-methyl-D-glucamine (MGD) [(Fe-MGD2)] was prepared by mixing $FeSO_4.7H_2O$ with MGD in degassed aqueous DMF (1:1) to final concentrations of 0.8 and 4 mM, respectively. Samples were maintained under a nitrogen atmosphere and in the absence of light until immediately before measurement. Samples were transferred to a hematocrit capillary, sealed, and placed in a quartz EPR tube to acquire the spectra. EPR spectra of photoNOD-1 or −2 (200 μM) were acquired either with or without 5 or 40 min irradiation at 680 or 690 nm in step-and-shoot mode, respectively (Figure S13). MAHMA-NONOate (a commercially available NO donor) was used as a positive control and for the preparation of the calibration curve. Varying concentrations were prepared in degassed 10 mM potassium hydroxide and quickly added to the Fe(II) complex (Figure S8). EPR spectra were recorded with a Varian E-line 12″ Century Series X-band CW EPR (VarianXBand) spectrometer at room temperature. Spectrometer settings: modulation frequency, 100 kHz; modulation amplitude, 2.5 G; gain, 4000; sweep width, 100 G; scan time, 0.5 min per scan, 6 scans, 3 min total; microwave power, 12 dB; and microwave frequency, 9.30 GHz. Additional information regarding the EPR materials can be found in the Supporting Information.

In Vivo Studies.

All *in vivo* experiments were performed with the approval of the Institutional Animal Care and Use Committee of the University of Illinois at Urbana–Champaign, following the principles outlined by the American Physiological Society on research animal use. Female BALB/c mice (5–7 weeks old) were acquired from The Jackson Laboratory. Hair was removed from the lower half of the body by shaving and applying depilatory cream prior to all experiments.

In Vivo NO Release and Monitoring.

Vehicle control or photoNODs (25 μL, 30 μM in sterile saline containing 2% DMSO) were injected subcutaneously into both flanks of BALB/c mice. PA images were acquired both before and after a 5 min period with irradiation (right flank) or without irradiation (left flank). Irradiation of photoNOD-1 and photoNOD-2 was performed at 710 and 700 nm, respectively, using step-and-shoot mode (120 angles, 39 pulses per angle, 4.8 min irradiation). Images were acquired at 710 and 810 nm for photoNOD-1 and 700 and 830 nm for photoNOD-2 using continuous rotation mode (6 s rotation time, 0.2 min irradiation).

Modulation of Tumor Progression Using photoNOD-1.

A suspension of 2.5×10^5 4T1 cells in serum-free medium containing 50% v/v Matrigel (50 μL) was injected subcutaneously into both flanks of BALB/c mice. Five days after tumor implantation, mice were randomly assigned to experimental and control groups. photoNOD-1 (1.2 mg/kg in 150 μL of sterile saline containing 20% DMSO) was administered to each mouse in the experimental group via retroorbital injection, while the control mice were treated with vehicle only. Four hours following administration, the left tumors of all mice were irradiated for 5 min using 700 nm light (step-and-shoot mode, 120 angles, 39 pulses per angle). PA images (700 and 830 nm) were acquired both before and after irradiation, and before and after a 5 min period without irradiation for the right tumors. This dosing session was repeated every other day for a total of 4 sessions. On treatment days, mice were weighed, and tumors were measured using calipers. Tumor volumes were calculated using the formula $V = (w^2 \times l)/2$, where w is the tumor width and l is the tumor length.[110,111]

Ex Vivo Biodistribution.

Tumor-bearing mice were treated with photoNOD-1 (1.2 mg/kg in 150 μL of sterile saline containing 20% DMSO) or vehicle without photoNOD-1 via retroorbital injection. After 4 h, mice were sacrificed and dissected to remove tissues of interest. Uptake of photoNOD-1 was determined via PA imaging (700 nm, continuous mode, 6 s rotation time) of individual organs in PBS. Custom regions of interest (ROIs) were drawn around each organ, and the mean ROI PA signal was determined.

Supplementary Material

Refer to Web version on PubMed Central for supplementary material.

■ ACKNOWLEDGMENTS

This work was supported by the Chemistry-Biology Interface Training Grant (T32 GM070421 to E.Y.Z. and C.J.R.), the Tissue Microenvironment Training Grant (T32 EB019944 to H.J.K.), the National Science Foundation Graduate Research Fellowship Program (NGE-1144245 to E.Y.Z.), the Spring-born Fellowship (to E.Y.Z.), the Beckman Fellowship (to H.J.K.), and the Alfred P. Sloan fellowship (FG-2017-8964 to J.C.). Major funding for the 500 MHz Bruker CryoProbeTM was provided by the Roy J. Carver Charitable Trust (Muscatine, Iowa; grant no. 15-4521) to the School of Chemical Sciences NMR Lab. The Q-Tof Ultima mass spectrometer was purchased in part with a grant from the National Science Foundation, Division of Biological Infrastructure (DBI-0100085). We also acknowledge the Core Facilities at the Carl R. Woese Institute for Genomic Biology for access to Leica CM3050S cryostat, tissue staining facility, and the Hamamatsu Photonics NanoZoomer Digital Pathology System.

■ REFERENCES

(1). Wang LV; Yao J Nat. Methods 2016, 13, 627–638. [PubMed: 27467726]

(2). Reinhardt CJ; Chan J Biochemistry 2018, 57, 194–199. [PubMed: 29022344]

(3). Heijblom M; Piras D; Brinkhuis M; van Hespen JCG; van den Engh FM; van der Schaaf M; Klaase JM; van Leeuwen TG; Steenbergen W; Manohar S Sci. Rep 2015, 5, 11778. [PubMed: 26159440]

(4). Yang M; Zhao L; He X; Su N; Zhao C; Tang H; Hong T; Li W; Yang F; Lin L; et al. Biomed. Opt. Express 2017, 8, 3449–3457. [PubMed: 28717580]

(5). Jo J; Xu G; Cao M; Marquardt A; Francis S; Gandikota G; Wang X Sci. Rep 2017, 7, 15026. [PubMed: 29101339]

(6). Liu Y; Zhang L; Li S; Han X; Yuan Z J. Biophotonics 2018, 11, e201700267. [PubMed: 29388738]

(7). Li H; Zhang P; Smaga LP; Hoffman RA; Chan J J. Am. Chem. Soc 2015, 137, 15628–15631. [PubMed: 26652006]

(8). Mishra A; Jiang Y; Roberts S; Ntziachristos V; Westmeyer GG Anal. Chem 2016, 88, 10785–10789. [PubMed: 27779396]

(9). Roberts S; Seeger M; Jiang Y; Mishra A; Sigmund F; Stelzl A; Lauri A; Symvoulidis P; Rolbieski H; Preller M; et al. J. Am. Chem. Soc 2018, 140, 2718–2721. [PubMed: 28945084]

(10). Knox HJ; Hedhli J; Kim TW; Khalili K; Dobrucki LW; Chan J Nat. Commun 2017, 8, 1794. [PubMed: 29176550]

(11). Knox HJ; Kim TW; Zhu Z; Chan J ACS Chem. Biol 2018, 13, 1838–1843. [PubMed: 29521492]

(12). Reinhardt CJ; Zhou EY; Jorgensen MD; Partipilo G; Chan J J. Am. Chem. Soc 2018, 140, 1011–1018. [PubMed: 29313677]

(13). Wang S; Li Z; Liu Y; Feng G; Zheng J; Yuan Z; Zhang X Sens. Actuators, B 2018, 267, 403–411.

(14). Kumara M; Jayakumar G; Idris NM; Zhang Y Proc. Natl. Acad. Sci. U. S. A 2012, 109, 8483. [PubMed: 22582171]

(15). Yan B; Boyer J-C; Habault D; Branda NR; Zhao Y J. Am. Chem. Soc 2012, 134, 16558–16561. [PubMed: 23013429]

(16). Goodman AM; Neumann O; Nørregaard K; Henderson L; Choi M-R; Clare SE; Halas NJ Proc. Natl. Acad. Sci. U. S. A 2017, 114, 12419–12424. [PubMed: 29109274]

(17). Rajaputra P; Bio M; Nkepang G; Thapa P; Woo S; You Y Bioorg. Med. Chem 2016, 24, 1540–1549. [PubMed: 26928287]

(18). Li H; Yang X; Zhou Z; Wang K; Li C; Qiao H; Oupicky D; Sun M J. Controlled Release 2017, 261, 126–137.

(19). Cheng Y; Doane TL; Chuang C-H; Ziady A; Burda C Small 2014, 10, 1799–1804. [PubMed: 24515950]

(20). Qiu M; Wang D; Liang W; Liu L; Zhang Y; Chen X; Sang DK; Xing C; Li Z; Dong B; et al. Proc. Natl. Acad. Sci. U. S. A 2018, 115, 501–506. [PubMed: 29295927]

(21). Anderson ED; Gorka AP; Schnermann MJ Nat. Commun 2016, 7, 13378. [PubMed: 27853134]

(22). Nagaya T; Gorka AP; Nani RR; Okuyama S; Ogata F; Maruoka Y; Choyke PL; Schnermann MJ; Kobayashi H Mol. Cancer Ther 2018, 17, 661–670. [PubMed: 29237807]

(23). Wang J; Liu Y; Ma Y; Sun C; Tao W; Wang Y; Yang X; Wang J Adv. Funct. Mater 2016, 26, 7516–7525.

(24). Kianfar E; Schäfer C; Lornejad-Schäfer MR; Portenkirchner E; Knör G Inorg. Chim. Acta 2015, 435, 174–177.

(25). Pierri AE; Huang P-J; Garcia JV; Stanfill JG; Chui M; Wu G; Zheng N; Ford PC Chem. Commun 2015, 51, 2072–2075.

(26). Nani RR; Gorka AP; Nagaya T; Kobayashi H; Schnermann MJ Angew. Chem., Int. Ed 2015, 54, 13635–13638.

(27). Jayakumar MKG; Idris NM; Zhang Y Proc. Natl. Acad. Sci. U. S. A 2012, 109, 8483–8488. [PubMed: 22582171]

(28). Zheng B; Su L; Pan H; Hou B; Zhang Y; Zhou F; Wu X; Gong X; Wang H; Chang J Adv. Mater 2016, 28, 707–714. [PubMed: 26619378]

(29). Yang Y; Liu F; Liu X; Xing B Nanoscale 2013, 5, 231–238. [PubMed: 23154830]

(30). Atilgan A; Tanriverdi Eçik E; Guliyev R; Uyar TB; Erbas-Cakmak S; Akkaya EU Angew. Chem., Int. Ed 2014, 53, 10678–10681.

(31). Denninger JW; Marletta MA Biochim. Biophys. Acta, Bioenerg 1999, 1411, 334–350.

(32). Bogdan C Nat. Immunol 2001, 2, 907–916. [PubMed: 11577346]

(33). Taylor E; Megson I; Haslett C; Rossi A Cell Death Differ. 2003, 10, 418–430. [PubMed: 12719719]

(34). Schairer DO; Chouake JS; Nosanchuk JD; Friedman AJ Virulence 2012, 3, 271–279. [PubMed: 22546899]

(35). Schulz R; Kelm M; Heusch G Cardiovasc. Res 2004, 61, 402–413. [PubMed: 14962472]

(36). Hirst D; Robson T J. Pharm. Pharmacol 2007, 59, 3–13. [PubMed: 17227615]

(37). Xu W; Liu LZ; Loizidou M; Ahmed M; Charles IG Cell Res. 2002, 12, 311–320. [PubMed: 12528889]

(38). Liu VWT; Huang PL Cardiovasc. Res 2008, 77, 19–29. [PubMed: 17658499]

(39). Hickok JR; Thomas DD Curr. Pharm. Des 2010, 16, 381–391. [PubMed: 20236067]

(40). Ignarro LJ; Napoli C; Loscalzo J Circ. Res 2002, 90, 21–28. [PubMed: 11786514]

(41). Wang PG; Xian M; Tang X; Wu X; Wen Z; Cai T; Janczuk AJ Chem. Rev 2002, 102, 1091–1134. [PubMed: 11942788]

(42). Xiang HJ; Guo M; Liu JG Transition-Metal Nitrosyls for Photocontrolled Nitric Oxide Delivery. European Journal of Inorganic Chemistry; Wiley-Blackwell: New York, 3 27, 2017; pp 1586–1595.

(43). Rose MJ; Mascharak PK Curr. Opin. Chem. Biol 2008, 12, 238–244. [PubMed: 18355461]

(44). Eroy-Reveles AA; Leung Y; Beavers CM; Olmstead MM; Mascharak PK J. Am. Chem. Soc 2008, 130, 6650–6650.

(45). Ostrowski AD; Deakin SJ; Azhar B; Miller TW; Franco N; Cherney MM; Lee AJ; Burstyn JN; Fukuto JM; Megson IL; et al. J. Med. Chem 2010, 53, 715–722. [PubMed: 19950902]

(46). Vuong C; Kocianova S; Yu J; Kadurugamuwa JL; Otto M J. Infect. Dis 2008, 198, 258–261. [PubMed: 18491976]

(47). de Lima RG; Sauaia MG; Bonaventura D; Tedesco AC; Bendhack LM; da Silva RS Inorg. Chim. Acta 2006, 359, 2543–2549.

(48). Makings LR; Tsien RY J. Biol. Chem 1994, 269, 6282–6285. [PubMed: 8119976]

(49). Namiki S; Arai T; Fujimori K J. Am. Chem. Soc 1997, 119, 3840–3841.

(50). Sortino S; Condorelli G; Marconi G Chem. Commun 2001, No. No. 13, 1226–1227.

(51). Suzuki T; Nagae O; Kato Y; Nakagawa H; Fukuhara K; Miyata N J. Am. Chem. Soc 2005, 127, 11720–11726. [PubMed: 16104749]

(52). Fukuhara K; Kurihara M; Miyata N J. Am. Chem. Soc 2001, 123, 8662–8666. [PubMed: 11535070]

(53). Karaki F; Kabasawa Y; Yanagimoto T; Umeda N; Firman; Urano Y; Nagano T; Otani Y; Ohwada T Chem. - Eur. J 2012, 18, 1127–1141. [PubMed: 22179925]

(54). Ieda N; Hotta Y; Miyata N; Kimura K; Nakagawa H J. Am. Chem. Soc 2014, 136, 7085–7091. [PubMed: 24731151]

(55). Kitamura K; Kawaguchi M; Ieda N; Miyata N; Nakagawa H ACS Chem. Biol 2016, 11, 1271–1278. [PubMed: 26878937]

(56). Blangetti M; Fraix A; Lazzarato L; Marini E; Rolando B; Sodano F; Fruttero R; Gasco A; Sortino S Chem. - Eur. J 2017, 23, 9026–9029. [PubMed: 28543638]

(57). Hishikawa K; Nakagawa H; Furuta T; Fukuhara K; Tsumoto H; Suzuki T; Miyata N J. Am. Chem. Soc 2009, 131, 7488–7489. [PubMed: 19438241]

(58). Nakagawa H; Hishikawa K; Eto K; Ieda N; Namikawa T; Kamada K; Suzuki T; Miyata N; Nabekura JI ACS Chem. Biol 2013, 8, 2493–2500. [PubMed: 23978195]

(59). He H; Ye Z; Xiao Y; Yang W; Qian X; Yang Y Anal. Chem 2018, 90, 2164–2169. [PubMed: 29316789]

(60). He H; Xia Y; Qi Y; Wang H-Y; Wang Z; Bao J; Zhang Z; Wu F-G; Wang H; Chen D; et al. Bioconjugate Chem. 2018, 29, 1194–1198.

(61). Zhang Z; Wu J; Shang Z; Wang C; Cheng J; Qian X; Xiao Y; Xu Z; Yang Y Anal. Chem 2016, 88, 7274–7280. [PubMed: 27297590]

(62). Xie X; Fan J; Liang M; Li Y; Jiao X; Wang X; Tang B Chem. Commun 2017, 53, 11941–11944.

(63). Svoboda K; Yasuda R Neuron 2006, 50, 823–839. [PubMed: 16772166]

(64). Wang LV; Yao J Nat. Methods 2016, 13, 627–638. [PubMed: 27467726]

(65). Fan W; Yung BC; Chen X Angew. Chem. Int. Ed 2018, 57, 2–14.

(66). Wecksler SR; Mikhailovsky A; Korystov D; Ford PC J. Am. Chem. Soc 2006, 128, 3831–3837. [PubMed: 16536559]

(67). Li H; Zhang P; Smaga LP; Hoffman RA; Chan J J. Am. Chem. Soc 2015, 137, 15628–15631. [PubMed: 26652006]

(68). Weber J; Beard PC; Bohndiek SE Nat. Methods 2016, 13, 639–650. [PubMed: 27467727]

(69). Komarov AM; Reef A; Schmidt HHH . Methods Enzymol 2002, 359, 18–27. [PubMed: 12481556]

(70). Yoshimura T; Kotake Y Antioxid. Redox Signaling 2004, 6, 639–647.

(71). Tricker AR; Preussmann R Mutat. Res. Genet. Toxicol. Test 1991, 259, 277–289.

(72). Barnes JM; Magee PN Occup. Environ. Med 1954, 11, 167–174.

(73). Magee PN; Barnes JM Br. J. Cancer 1956, 10, 114–122. [PubMed: 13342328]

(74). Bogovski P; Bogovski S Int. J. Cancer 1981, 27, 471–474. [PubMed: 7275353]

(75). Ciancio G; Pollack A; Taupier MA; Block NL; Irvin GL J. Histochem. Cytochem 1988, 36, 1147–1152. [PubMed: 2457047]

(76). Breier JM; Radio NM; Mundy WR; Shafer TJ Toxicol. Sci 2008, 105, 119–133. [PubMed: 18550602]

(77). Evans MA; Huang P-J; Iwamoto Y; Ibsen KN; Chan EM; Hitomi Y; Ford PC; Mitragotri S Chem. Sci 2018, 9, 3729–3741. [PubMed: 29780505]

(78). Tesei A; Ulivi P; Fabbri F; Rosetti M; Leonetti C; Scarsella M; Zupi G; Amadori D; Bolla M; Zoli W J. Transl. Med 2005, 3, 7. [PubMed: 15691389]

(79). Wu S-C; Lu C-Y; Chen Y-L; Lo F-C; Wang T-Y; Chen Y-J; Yuan S-S; Liaw W-F; Wang Y-M Inorg. Chem 2016, 55, 9383–9392. [PubMed: 27572677]

(80). Lee SY; Rim Y; McPherson DD; Huang SL; Kim H Biomed. Mater. Eng 2014, 24, 61–67. [PubMed: 24211883]

(81). Garbàn HJ; Bonavida B J. Biol. Chem 2001, 276, 8918–8923. [PubMed: 11118442]

(82). Huerta-Yepez S; Vega M; Jazirehi A; Garban H; Hongo F; Cheng G; Bonavida B Oncogene 2004, 23, 4993–5003. [PubMed: 15048072]

(83). Bonavida B; Baritaki S; Huerta-Yepez S; Vega MI; Chatterjee D; Yeung K Nitric Oxide 2008, 19, 152–157. [PubMed: 18477483]

(84). Bonavida B; Garban H Redox Biol. 2015, 6, 486–494. [PubMed: 26432660]

(85). Ostrowski AD; Ford PC Dalt. Trans 2009, 10660.

(86). Guo R; Tian Y; Wang Y; Yang W Adv. Funct. Mater 2017, 27, 1606398.

(87). Mitchell JB; Wink DA; Degraff W; Gamson J; Keefer LK; Krishna MC Cancer Res. 1993, 53, 5845–5848. [PubMed: 8261391]

(88). Griffin RJ; Makepeace CM; Hur W-J; Song CW Int. J. Radiat. Oncol. Biol. Phys 1996, 36, 377–383. [PubMed: 8892463]

(89). Chung P; Cook T; Liu K; Vodovotz Y; Zamora R; Finkelstein S; Billiar T; Blumberg D Nitric Oxide 2003, 8, 119–126. [PubMed: 12620375]

(90). Cook T; Wang Z; Alber S; Liu K; Watkins SC; Vodovotz Y; Billiar TR; Blumberg D Cancer Res. 2004, 64, 8015–8021. [PubMed: 15520210]

(91). Jordan BF; Sonveaux P; Feron O; Grégoire V; Beghein N; Dessy C; Gallez B Int. J. Cancer 2004, 109, 768–773. [PubMed: 14999787]

(92). Yardeni T; Eckhaus M; Morris HD; Huizing M; Hoogstraten-Miller S Lab Anim. (NY) 2011, 40, 155–160. [PubMed: 21508954]

(93). Berezin MY; Guo K; Akers W; Livingston J; Solomon M; Lee H; Liang K; Agee A; Achilefu S Biochemistry 2011, 50, 2691–2700. [PubMed: 21329363]

(94). Zhang L; Bhatnagar S; Deschenes E; Thurber GM Sci. Rep 2016, 6, 25424. [PubMed: 27147293]

(95). National Research Council. Recogition Ond Alleviation of Pain and Distress in Laboratory Animals; National Academies Press: Washington, DC, 1992.

(96). Walker MW; Kinter MT; Roberts RJ; Spitz DR Pediatr. Res 1995, 37, 41–49. [PubMed: 7700733]

(97). Le X; Wei D; Huang S; Lancaster JR; Xie K Proc. Natl. Acad. Sci. U. S. A 2005, 102, 8758–8763. [PubMed: 15939886]

(98). Villalobo A FEBS J. 2006, 273, 2329–2344. [PubMed: 16704409]

(99). Xia J; Kim C; Lovell JF Curr. Drug Targets 2015, 16, 571–581. [PubMed: 26148989]

(100). Lee HJ; Liu Y; Zhao J; Zhou M; Bouchard RR; Mitcham T; Wallace M; Stafford RJ; Li C; Gupta S; et al. J. Controlled Release 2013, 172, 152–158.

(101). Bao T; Yin W; Zheng X; Zhang X; Yu J; Dong X; Yong Y; Gao F; Yan L; Gu Z; et al. Biomaterials 2016, 76, 11–24. [PubMed: 26517561]

(102). Song X-R; Wang X; Yu S-X; Cao J; Li S-H; Li J; Liu G; Yang H-H; Chen X Adv. Mater 2015, 27, 3285–3291. [PubMed: 25885638]

(103). Liu J; Wang C; Wang X; Wang X; Cheng L; Li Y; Liu Z Adv. Funct. Mater 2015, 25, 384–392.

(104). Wang T; Wang D; Yu H; Wang M; Liu J; Feng B; Zhou F; Yin Q; Zhang Z; Huang Y; et al. ACS Nano 2016, 10, 3496–3508. [PubMed: 26866752]

(105). Zhang R; Fan Q; Yang M; Cheng K; Lu X; Zhang L; Huang W; Cheng Z Adv. Mater 2015, 27, 5063–5069. [PubMed: 26222210]

(106). Yang Z; Dai Y; Yin C; Fan Q; Zhang W; Song J; Yu G; Tang W; Fan W; Yung BC; et al. Adv. Mater 2018, 30, 1707509.

(107). Jung E; Kang C; Lee J; Yoo D; Hwang DW; Kim D; Park S-C; Lim SK; Song C; Lee D ACS Nano 2018, 12, 392–401. [PubMed: 29257881]

(108). Wecksler S; Mikhailovsky A; Ford PC J. Am. Chem. Soc 2004, 126, 13566–13567. [PubMed: 15493884]

(109). Li H; Wan A Analyst (Cambridge, U. K.) 2015, 140, 7129–7141.

(110). Euhus DM; Hudd C; Laregina MC; Johnson FE J. Surg. Oncol 1986, 31, 229–234. [PubMed: 3724177]

(111). Tomayko MM; Reynolds CP Cancer Chemother. Pharmacol 1989, 24, 148–154. [PubMed: 2544306]

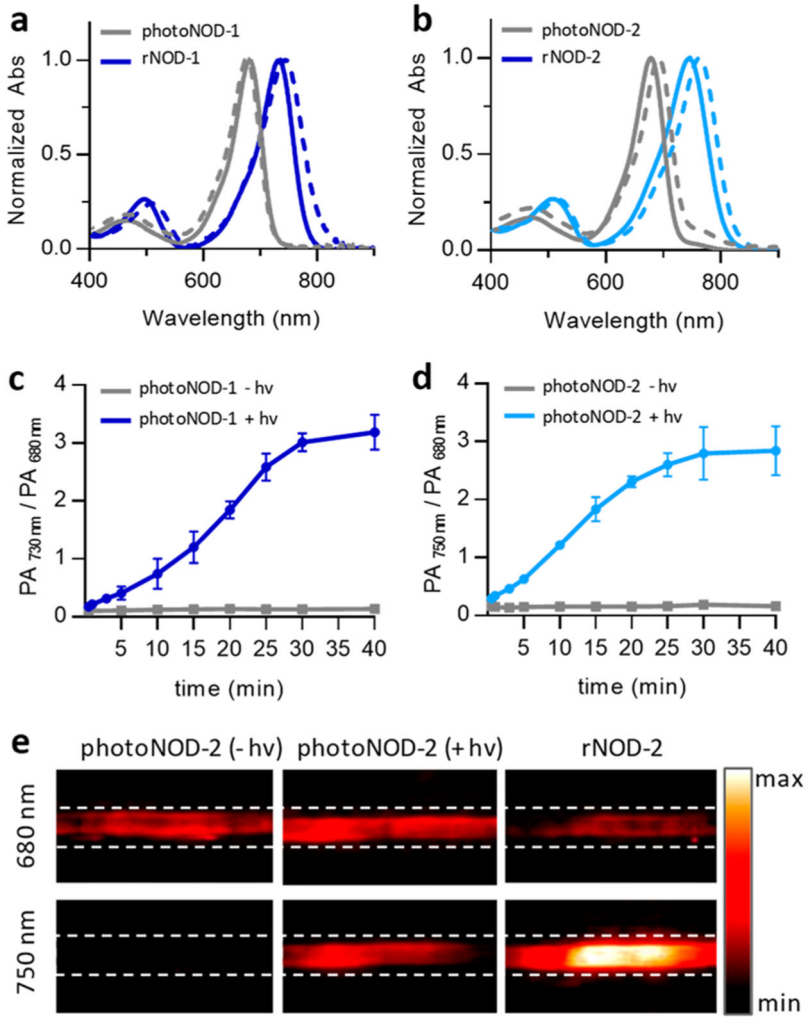

Figure 1.

(a) Absorbance spectra of photoNOD-1 and rNOD-1 and (b) photoNOD-2 and rNOD-2 in $CHCl_3$ (solid line) and aqueous buffer (dashed line; photoNOD-1: 50% EtOH/HEPES, pH 7.4; photoNOD-2: 0.1% CrEL/HEPES, pH 7.4). (c) In vitro PA monitoring of 10 μM photoNOD-1 ($PA_{730\ nm}/PA_{680\ nm}$) and (d) photoNOD-2 ($PA_{750\ nm}/PA_{680\ nm}$) turnover upon irradiation at 680 nm in $CHCl_3$ in tissue-mimicking phantoms. Data presented as mean ± SD ($n = 3$). (e) Representative PA images of photoNOD-2 (10 μM) without irradiation (left), after 5 min of irradiation (center), and an authentic sample of rNOD-2 shown for comparison (right) in tissue-mimicking phantoms.

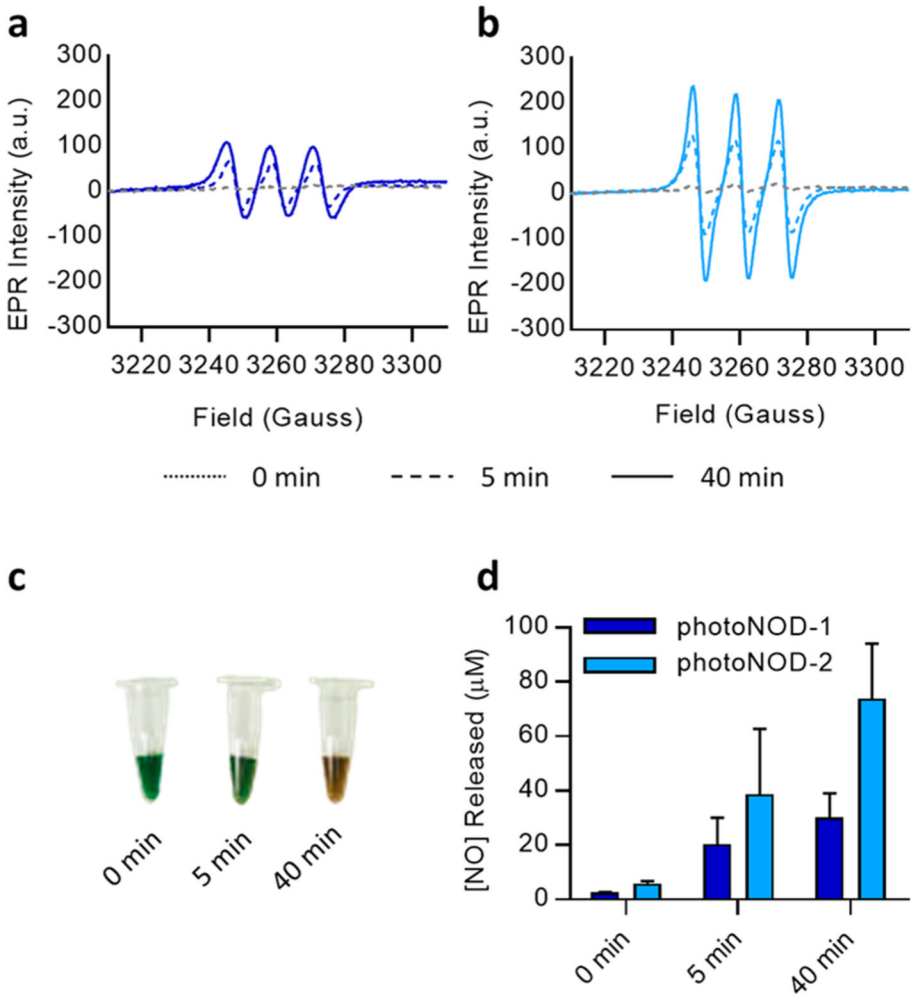

Figure 2.

EPR spectra collected after 0, 5, and 40 min of irradiation of (a) photoNOD-1 (690 nm) or (b) photoNOD-2 (680 nm) (200 μM in water containing 50% DMF) in the presence of $Fe(MGD)_2$. (c) Representative images showing colorimetric change of the EPR samples at each time point. (d) Quantification of NO release. Data presented as mean ± SD (n = 3).

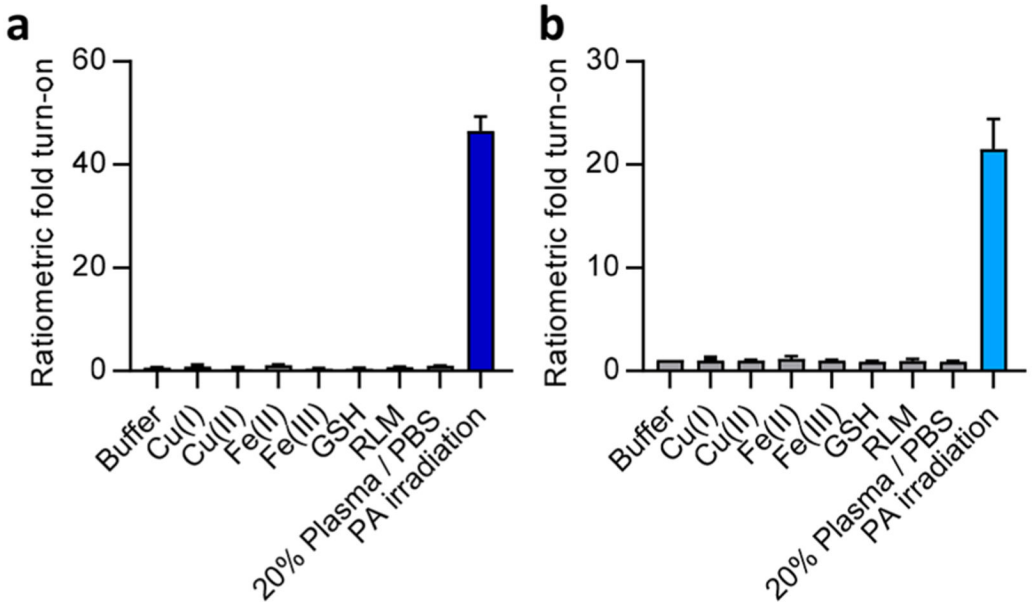

Figure 3.

Ratiometric fold turn-on of (a) photoNOD-1 and (b) photoNOD-2 (5 μM) upon exposure to redox-active metals (20 μM), glutathione (1 mM), rat liver microsomes (10 μL, 200 μ/mL final concentration with 5 μM NADPH), plasma, and irradiation at λ_{blue} at 37 °C in aqueous buffers (photoNOD-1:50% EtOH/HEPES, pH 7.4; photoNOD-2:0.1% CrEL/HEPES, pH 7.4). Data presented as mean ± SD (n = 3).

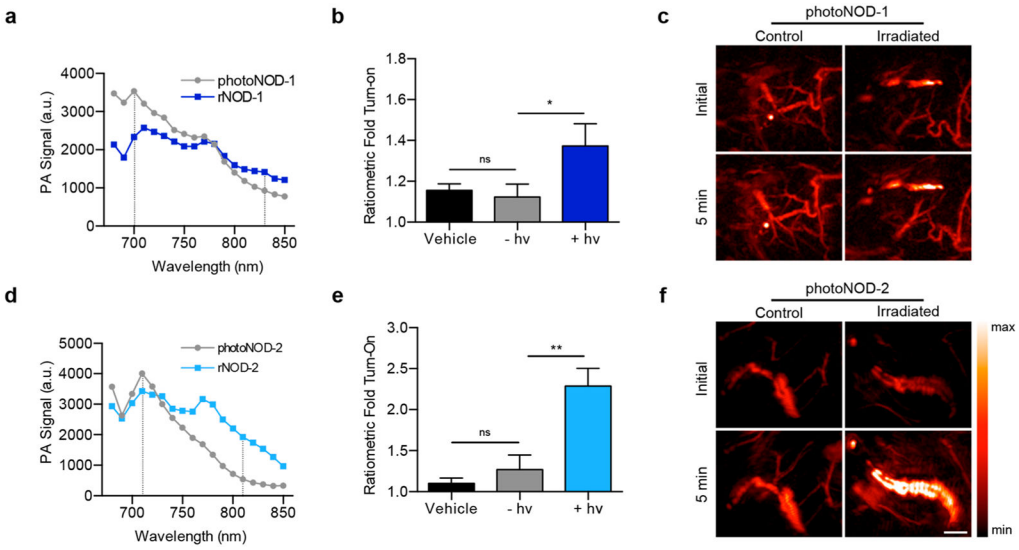

Figure 4.

(a) *In vivo* PA spectra of photoNOD-1 and rNOD-1 after injection into the flank. Dashed lines indicate wavelengths selected for ratiometric imaging. (b) Ratiometric fold turn-on of vehicle control without irradiation and photoNOD-1 after injection and a 5 min period with/without irradiation at λ_{PAbble} (700 nm) and (c) representative PA images at λ_{PAred} (830 nm). (d) *In vivo* PA spectra of photoNOD-2 and rNOD-2 after injection into the flank. Dashed lines indicate wavelengths selected for ratiometric imaging. (e) Ratiometric fold turn-on of vehicle control without irradiation and photoNOD-2 after injection and a 5 min period with/without irradiation at λ_{PAbble} (710 nm) and (f) representative PA images at λ_{PAred} ($n = 3$). photoNODs were administered via subcutaneous injection (25 μL, 30 μM in sterile saline with 2% DMSO). Scale bars represent 2.0 mm. Each set of images has been adjusted to the same contrast for comparison. Data presented as mean ± SD ($n = 3$ for (b),(e)). *$p < 0.05$, **$p < 0.01$.

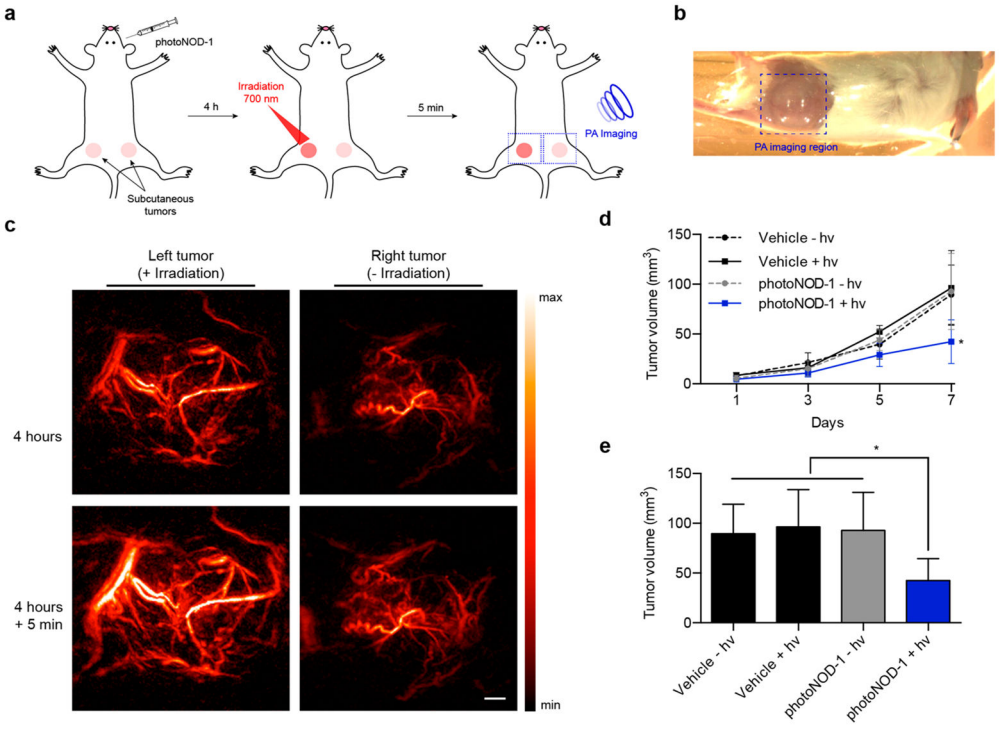

Figure 5.

(a) Schematic illustration of photoNOD-1 administration and NO release with PA monitoring. (b) Photograph of mouse in the imaging tray of the PA tomographer. Dashed line indicates region of PA imaging. (c) PA images (λ_{PAred}) acquired before/after a 5 min period with/without irradiation ($\lambda_{\mathrm{PAblue}}$) 4 h following systemic administration of photoNOD-1 (1.2 mg/kg, 150 μL, 20% DMSO in sterile saline). Both sets of images are adjusted to identical contrast for comparison. (d) Tumor volumes measured by calipers on each day of treatment. (e) Tumor volumes measured by calipers on day 7 of treatment. Scale bar represents 2.0 mm. Data presented as mean ± SD ($n \geq 3$). *$p < 0.05$.

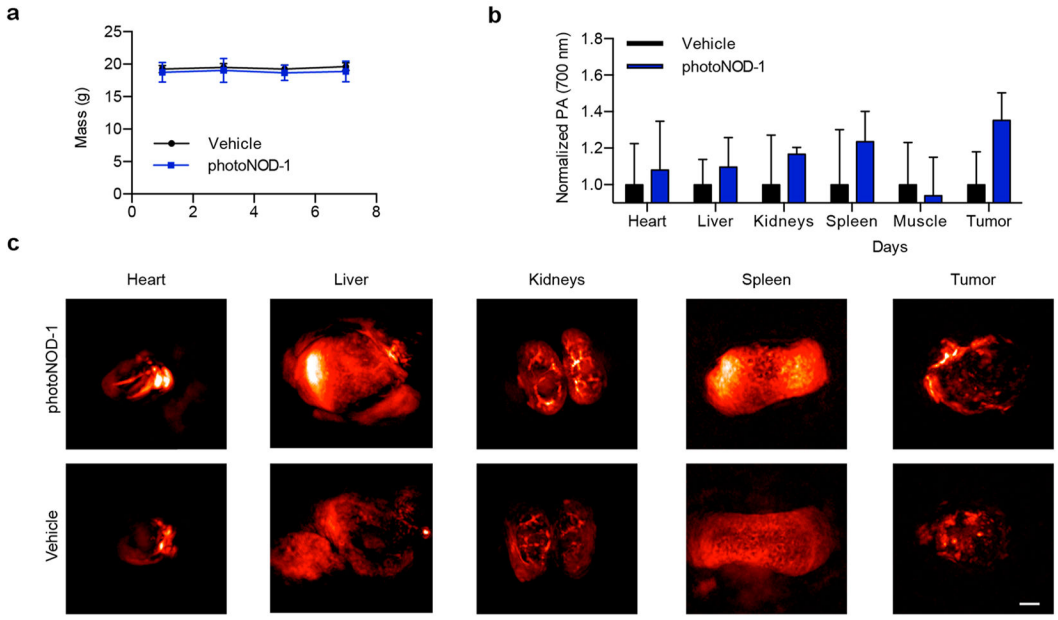

Figure 6.

(a) PA signal (λ_{PAblue}) of various mouse tissues. Mice were sacrificed, and tissues were removed for imaging 4 h following retroorbital injection of photoNOD-1 (1.2 mg/kg, 150 μL, 20% DMSO in sterile saline) or vehicle control ($n \geq 3$). Signals are normalized to average control values for comparison. (b) Mouse weight for photoNOD-treated and control animals measured on each treatment day ($n \geq 3$). (c) Representative PA images (λ_{PAblue}) of various tissues of mice treated with photoNOD-1 or vehicle control. Scale bar represents 2.0 mm.

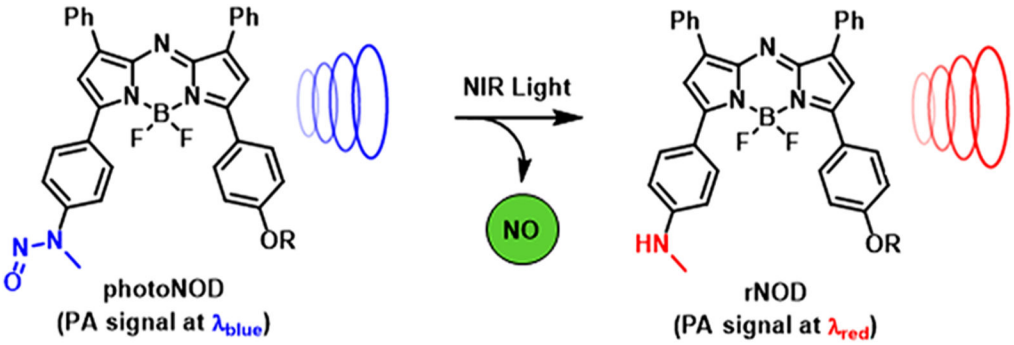

Scheme 1.

Irradiation of photoNOD Generates NO with Concomitant Release of rNOD, Which Can Be Monitored by Ratiometric PA Imaging

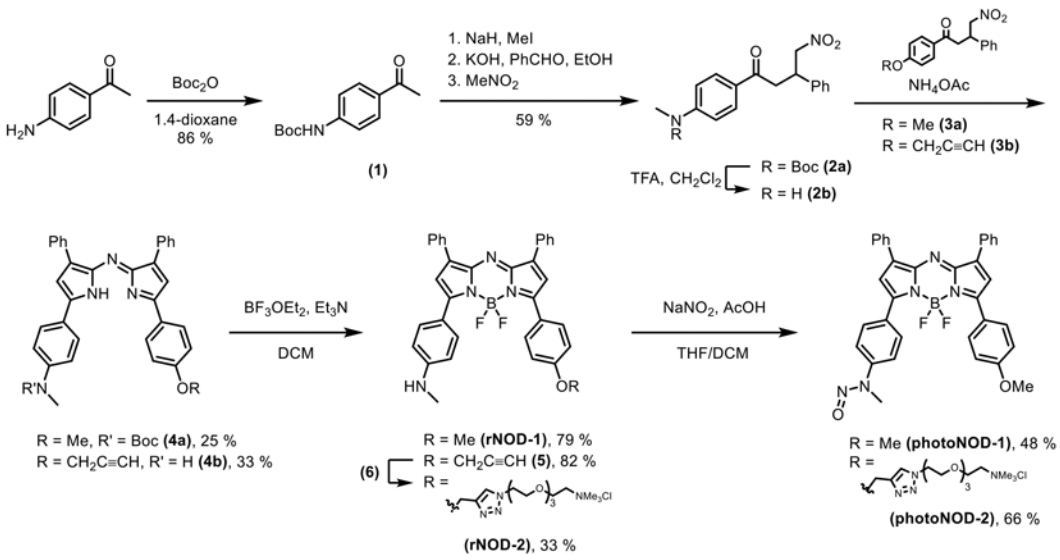

Scheme 2.

Synthesis of rNOD-1, rNOD-2, photoNOD-1, and photoNOD-2

Table 1.

λ_{red} and λ_{blue} (in nm) in Various Solvent Systems[a]

species	$\lambda_{blue}/\lambda_{red}$ (a)	$\lambda_{blue}/\lambda_{red}$ (b)
photoNOD/rNOD-1	681/733	677/746
photoNOD/rNOD-2	678/745	691/762

[a]Chloroform (a) and aqueous buffer (b): photoNOD-1: 50% EtOH/HEPES, pH 7.4; photoNOD-2: 0.1% CrEL/HEPES, pH 7.4.